Hindawi Publishing Corporation
International Journal of Optics
Volume 2012, Article ID 157319, 12 pages
doi:10.1155/2012/157319

Review Article

Manipulating the Propagation of Solitons with Solid-Core Photonic Bandgap Fibers

O. Vanvincq, A. Kudlinski, A. Bétourné, A. Mussot, Y. Quiquempois, and G. Bouwmans

Laboratoire PhLAM, UMR CNRS 8523, IRCICA, Université Lille 1, 59655 Villeneuve d'Ascq Cedex, France

Correspondence should be addressed to A. Kudlinski, alexandre.kudlinski@univ-lille1.fr

Received 7 April 2011; Accepted 20 June 2011

Academic Editor: Miguel González Herráez

We review the dynamics of soliton self-frequency shift induced by Raman gain in special solid-core photonic bandgap fibers and its consequences in terms of supercontinuum generation. These photonic bandgap fibers have been designed to allow nonlinear experiments in the first bandgap without suffering from significant loss even when working close to the photonic bandgap edge. We studied experimentally, numerically, and analytically the extreme deceleration of the soliton self-frequency shift at the long-wavelength edge of the first transmission window. This phenomenon is interpreted as being due to a large variation of the group-velocity dispersion in this spectral range and has been obtained with no significant power loss. Then, we investigated experimentally and numerically the generation of supercontinuum in this kind of fibers, in both spectral and temporal domains. In particular, we demonstrated an efficient tailoring of the supercontinuum spectral extension as well as a strong noise reduction at its long-wavelength edge.

1. Introduction

Solid-core photonic bandgap (PBG) fibers are one class of microstructured optical fibers in which light is confined in a low-index solid core by the PBGs of the cladding [1]. In the case of two-dimensional PBGs, the periodic microstructured cladding is usually composed of periodic high-index inclusions embedded in a low-index background [1]. The core region then corresponds to a defect (lack of inclusion) in the center of the periodic structure. Because of the intrinsic nature of the PBG waveguidance, the fiber transmission properties are characterized by discrete spectral bands [1, 2] in which the group-velocity dispersion (GVD), attenuation, and effective mode area of the fundamental core mode are strongly wavelength dependent [3], especially near the PBG edges [1, 4]. These singular characteristics are thus of particular interest in the field of nonlinear (NL) fiber optics. The potential of solid-core PBG fibers for NL propagation experiments has already been pointed out by the report of soliton propagation and phase-matched dispersive wave generation [5, 6], even across different PBG [7]. Degenerate four-wave mixing [8], frequency doubling and tripling [9], and supercontinuum (SC) generation across adjacent PBGs have also been investigated numerically [10].

In this paper, we present an overview of our recent work showing how the particular properties of solid-core PBG fibers can influence soliton propagation and SC generation. First, we detail the linear properties of the fabricated solid-core PBG fibers under investigation through experiments and numerical modelling. Then, we demonstrate experimentally that the soliton self-frequency shift (SSFS) effect can be strongly mitigated [11]. A simple analytical model indicates that this is caused by the strong third-order dispersion experienced by solitons as they approach the PBG edge. Finally, we show that this SSFS quasicancellation allows to control the spectral extent of infrared SC in the long-pulse regime [12] and, simultaneously, leads to a significant reduction of spectral power fluctuations at the SC long-wavelength edge [13].

2. Linear Properties of the Solid-Core Photonic Bandgap Fibers

The solid-core PBG fibers used in various experiments reported in this paper are all based on the same double periodicity structure [11, 12], although their optogeometrical characteristics (summarized in Table 1) slightly vary from one fiber to another. The scanning electron microscope

Table 1: Table summarizing the optogeometrical properties of the three fabricated solid-core PBG fibers under investigation.

	d_{Ge} (μm)	d_{air} (μm)	Λ (μm)	ZDW (nm)	NL coefficient ($W^{-1}\cdot km^{-1}$)	PBG edge (nm)
Fiber 1	2.19	2.33	3.09	905	6 (at 1200 nm)	1535
Fiber 2	2.20	2.25	3.25	915	6.9 (at 1064 nm)	1580
Fiber 3	2.22	2.27	3.28	921	6.8 (at 1064 nm)	1590

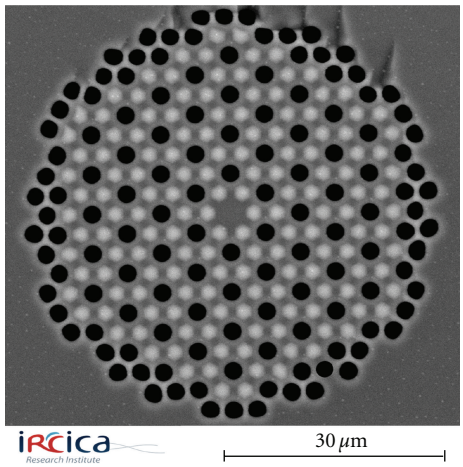

Figure 1: SEM image of the solid-core PBG fiber 1. Black regions are air holes, light gray regions are GeO_2-doped inclusions, and the dark gray background is pure silica.

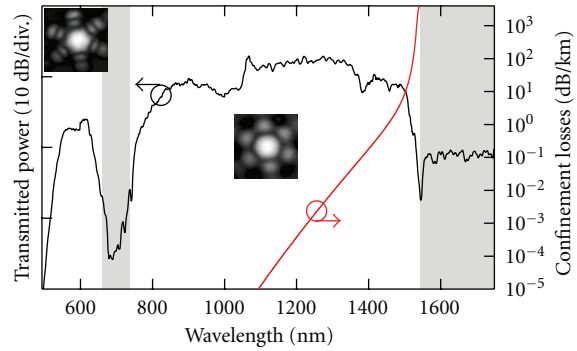

Figure 2: Transmission spectrum of the solid-core PBG fiber 1 (black line, left axis) measured with a SC source, and computed confinement losses across the first PBG (red line, right axis). Insets show the near-field mode profile in the first (right) and second (left) PBG. Gray areas depict spectral regions in which the PBG guidance in the core is not allowed.

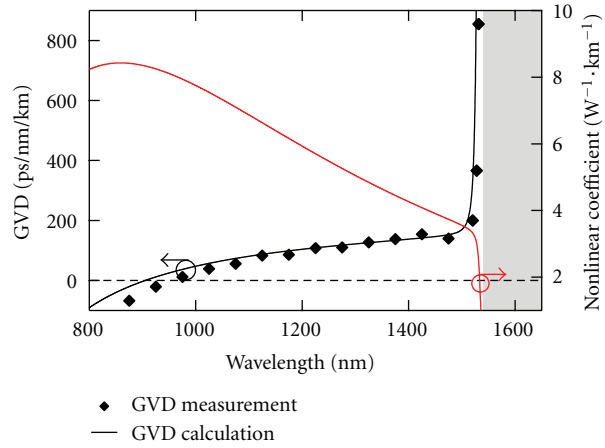

Figure 3: Calculated GVD curve of the solid-core PBG fiber 1 (solid black line, left axis), and corresponding measurements with a white-light interferometry setup (markers). Spectral evolution of the computed NL coefficient (red line, right axis). The gray area depicts the region outside the first PBG transmission window.

(SEM) image shown in Figure 1 illustrates such a double periodicity solid-core PBG fiber. The periodical high-index resonators (light gray regions in Figure 1) present in the cladding are responsible for the PBG guidance and are made of germanium-doped silica with a parabolic refractive index profile and a maximal index difference Δn of 32×10^{-3} (as compared to pure silica). They are embedded in a pure silica background (dark gray). Because we decided to work in the first PBG (mainly to minimize the effective area in order to maximize the NL coefficient), air holes of diameter d_{air} (depicted in black in Figure 1) were periodically added into the cladding structure for reducing the otherwise relatively high confinement losses in this PBG [14, 15]. The core region corresponds to a defect (lack of air hole) in the center of the periodic structure. The geometrical parameters of the three solid-core PBG fibers investigated here are summarized in Table 1, where the pitch Λ corresponds to the distance between two neighboring germanium-doped inclusions.

Although all fibers were characterized the same way, we only present here the linear properties of fiber 1, whose SEM image is depicted in Figure 1. Other fibers present similar characteristics, with a slight red-shift of the PBG transmission windows due to a slightly greater pitch Λ. Figure 2 shows the experimental transmission spectrum of a white light SC source through a 2 m long sample of the solid-core PBG fiber. The first PBG is very broad and extends from 740 to 1535 nm, whereas the second one is much sharper and extends from 510 to 650 nm. As for usual solid-core PBG fibers, typical resonances can be observed in the first ring of high-index resonators [4], with the number of intensity maxima indicating the PBG order (insets of Figure 2). The red curve (right axis) shows confinement losses across the first PBG calculated with a finite element mode solver. They are less than 1 dB/km across most of the PBG, and as expected they drastically increase to the dB/m range near the PBG edge. Figure 3 shows the calculated GVD curve of the solid-core PBG fiber 1 (solid black line), as well as measurements

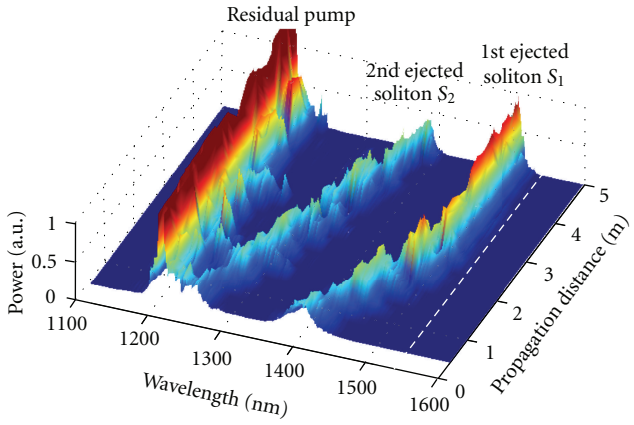

FIGURE 4: Evolution of the experimental output spectrum (linear scale) with fiber length (from 0.4 to 5 m) for 270 fs pump pulses at 1200 nm. The white dashed line represents the PBG edge.

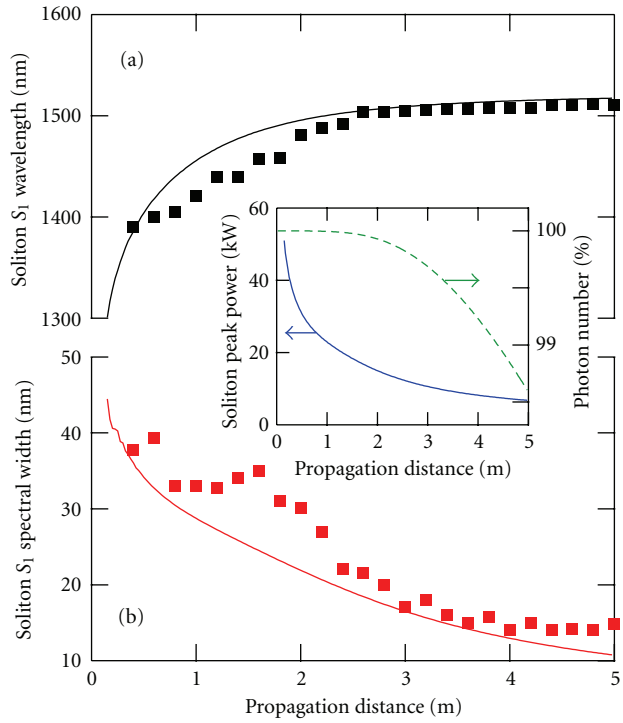

FIGURE 5: (a) Central wavelength of the first ejected soliton S_1 as a function of propagation distance. (b) Evolution of the soliton S_1 spectral width as a function of propagation distance. Solid lines and markers, respectively, correspond to numerical simulations and experimental measurements. Inset: numerical simulation of soliton S_1 peak power (blue solid line, left axis) and of the total photon number (green dashed line, right axis) versus propagation distance.

(markers) performed with a low coherence interferometric method [16]. The GVD slightly increases from the zero-dispersion wavelength (ZDW), located around 900 nm, to about 200 ps/nm/km at 1510 nm. For higher wavelengths, the GVD increase suddenly becomes much more important because of an anticrossing point between the fundamental core mode and cladding modes at 1535 nm, delimiting the practical PBG transmission window [12]. In this region near the PBG edge, the GVD reaches extreme values well higher than 1000 ps/nm/km: measurements (not displayed in Figure 3 for the sake of clarity) indicates a GVD value 4760 ps/nm/km at 1535 nm, in excellent agreement with the calculated curve. This leads the third-order dispersion β_3 to reach extremely high values in the order of 10^{-37} s^3/m in this spectral region. Finally, we also studied numerically the spectral dependance of the NL coefficient γ defined as $\gamma = n_2\omega/cA_{\text{eff}}$ [17], with n_2 the NL refractive index of pure silica and A_{eff} the mode effective area. Because the effective area also increases strongly near the PBG edge (due to the anticrossing phenomenon), the NL coefficient γ decreases rapidly near the PBG edge (see red curve in Figure 3) from about 6 W$^{-1}\cdot$km^{-1} at 1200 nm to less than 1.3 W$^{-1}\cdot$km^{-1} at 1535 nm.

In the following, we will see that the strong and unusual spectral dependencies of GVD and NL coefficient near the PBG edge can be used to tailor and manipulate the propagation of solitons approaching this spectral region through SSFS, included in the context of long-pulse SC generation.

3. Quasicancellation of the Soliton Self-Frequency Shift

3.1. Experimental Evidence. To illustrate this possible manipulation of the SSFS, NL propagation experiments were first performed by launching 270 fs pulses with a repetition rate of 1 kHz at 1200 nm into a 5 m long sample of the solid-core PBG fiber 1. This pump wavelength has been chosen from a compromise between a wavelength not too close to the long-wavelength edge of the first PBG (in order to observe a significant SSFS) and not too close to the ZDW (in order to avoid SC generation). Similarly, the input peak power was adjusted so that it was high enough to observe SSFS for several solitons while being low enough to avoid SC generation. The pump peak power effectively launched into the fiber core was estimated to about 10–20 kW. Figure 4 shows a representation of the output spectrum (in linear scale) as a function of fiber length from 0.4 to 5 m. It was obtained from a cut-back measurement in which the output spectrum was recorded every 20 cm while keeping the launch conditions unchanged. The input Gaussian pulse breaks up into two fundamental solitons (labeled S_1 and S_2) through a fission mechanism [18, 19] caused by Raman scattering and higher-order dispersion effects [19, 20]. As expected, both solitons then red-shift through Raman-induced SSFS [21, 22]. The most striking feature in the soliton dynamics is that, after 2.5 m, the first ejected soliton, S_1, becomes frequency locked at a central wavelength of about 1510 nm, that is, when its spectrum starts to overlap with the PBG located at 1535 nm (depicted in white dotted line in Figure 4). This is even more clearly illustrated in Figure 5(a) which shows a plot of the S_1 soliton central wavelength (black squares) as a function of the propagation distance. A clear slope change in the SSFS rate is observed at the fiber length of 2.5 m. Red squares in Figure 5(b) represent the evolution of soliton S_1 full width at half maximum (FWHM) spectral width versus

propagation length. It is shown that, as soliton S_1 red-shifts, it initially experiences a spectral compression from about 40 nm to 15 nm within the first 3 m. For longer propagation distances, that is, when the soliton is frequency locked, its spectral width stabilizes to about 15 nm, without any significant change in its spectral power density, as observed in Figure 4. Note that the same phenomenon was observed for the soliton S_2 (at a longer fiber length) and even for more than five ejected solitons by increasing the pump power. These experiments clearly show that the SSFS is extremely decelerated (and even quasicancelled) when the solitons approach the PBG edge, this effect being accompanied by a spectral compression.

3.2. Confirmation with Numerical Simulations. In order to get further insight into this phenomenon, we performed numerical simulations by integrating the generalized NL Schrödinger equation (GNLSE) taking into account the mode profile dispersion [23]. In this case, it writes [23, 24]:

$$\frac{\partial \widetilde{C}(z,\omega)}{\partial z} = i(\beta(\omega)-\beta_0-\beta_1(\omega-\omega_0))\widetilde{C}(z,\omega)-\frac{\alpha(\omega)}{2}\widetilde{C}(z,\omega) + i\overline{\gamma}(\omega)\mathcal{F}\left(C(z,t)\int_{-\infty}^{\infty}R(t-t')\,|\,C(z,t')\,|^2dt'\right), \quad (1)$$

where the NL coefficient takes the following form [24]:

$$\overline{\gamma}(\omega)=\frac{n_2\omega n_0}{cn_{\text{eff}}(\omega)\sqrt{A_{\text{eff}}(\omega)A_{\text{eff}}(\omega_0)}} \quad (2)$$

and $\widetilde{C}(z,\omega)=\widetilde{A}(z,\omega)(A_{\text{eff}}(\omega_0)/A_{\text{eff}}(\omega))^{1/4}$, $\widetilde{A}(z,\omega)$ being the complex spectral envelope. The coefficient β_0 corresponds to the mode propagation constant $\beta(\omega)$ at the center frequency of the input pulse spectrum ω_0, and β_1 is the first derivative of $\beta(\omega)$ (i.e., $d\beta(\omega)/d\omega$). The symbol $\mathcal{F}$ denotes the Fourier transform of the function in argument, and $\alpha(\omega)$ is the fiber linear power attenuation at ω. The silica response function is defined by $R(t)=(1-f_R)\delta(t)+f_Rh_R(t)$ where $f_R=0.18$ and $h_R(t)$ is the Raman response function which is approximated by the analytical expression given in [25].

Figure 6 shows a propagation simulation over 5 m of a 270 fs Gaussian pulse with 15 kW peak power centered at 1200 nm, corresponding to the input experimental pulses. The frequency dependence of all parameters, that is, $\alpha(\omega)$, $\beta(\omega)$, and $A_{\text{eff}}(\omega)$, associated with the experimental fiber was taken into account. This simulation shows excellent qualitative agreement with the experimental results of Figure 4. The input pulse experiences fission leading to the ejection of two fundamental solitons, labeled S_1 to S_2, and the SSSF associated to soliton S_1 is strongly decelerated near the PBG edge. This effect is accompanied by a spectral compression and an increase of its spectral power density. Black and red solid lines in Figure 5, respectively, correspond to the simulated soliton S_1 central wavelength and FWHM spectral width. They show good quantitative agreement with experiments, especially when the solitons approach the PBG edge (for propagation distances greater than 2.5 m). The blue solid curve in the inset of Figure 5 represents the soliton S_1 peak power as a function of propagation distance. Although its spectral power density increases (as shown in Figure 6), its peak power (in the temporal domain) decreases along propagation, because the soliton temporally broadens. The variation of total photon number as a function of fiber length is displayed in the green dashed curve in the inset of Figure 5. It decreases (due to linear attenuation) by only less than 1.5% within the first 5 m, which indicates that the soliton S_1 does not significantly suffer from the high attenuation at the PBG edge. This suggests that the quasicancellation of the SSFS does not occur at the expense of significant attenuation. At this point, however, the physics at the origin of this phenomenon has not been elucidated yet.

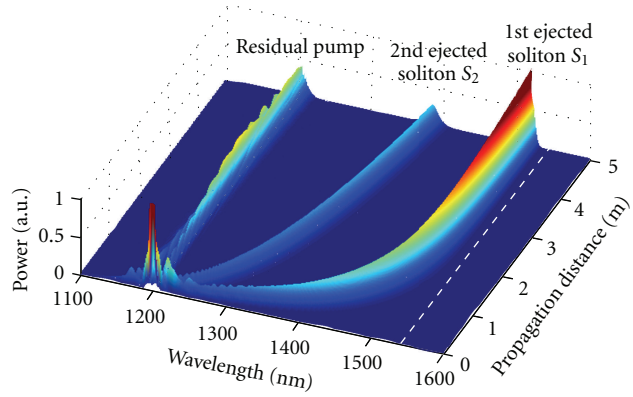

Figure 6: Numerical simulation of the propagation of a 270 fs Gaussian pulse with 15 kW peak power centered at 1200 nm, showing fission and ejection of two fundamental solitons S_1 and S_2. All frequency-dependant parameters of the fiber were taken into account. The white dashed line represents the PBG edge.

3.3. Discussion. First, let us recall that, as a soliton reaches the PBG edge, the values of the GVD evaluated at its central frequency strongly increase while its NL coefficient is largely reduced (see Figure 3). All these spectral evolutions are expected to be detrimental to the efficiency of the SSFS as they lead, directly or indirectly, to a significant increase of the pulse duration which is known to strongly affect the SSFS efficiency [17, 22]. In the following, we will present an analytical approach that allows to quantify the relative weight of the spectral dependence of the GVD ($d\beta_2/d\omega$) and NL coefficient ($d\overline{\gamma}/d\omega$) on the SSFS rate. For the sake of clarity, we only consider hereafter fundamental solitons as input pulses. This is justified by the fact that experimental input pulses experience fission which leads to pulse breakup and ejection of actual fundamental solitons [18–20]. The characteristics of these input pulses (hyperbolic secant pulses of 21 fs duration FWHM and 100 kW peak power) were estimated from the measurement of the soliton S_1 spectral width in Figure 5(b), assuming a soliton order $N^2=1$.

The starting point of our analysis is the well-known Gordon formula allowing to predict the SSFS rate, $d\langle\omega\rangle/dz$, of a fundamental soliton of mean frequency $\langle\omega\rangle$ and

duration T as a function of propagation distance z [22]. It writes

$$\frac{d\langle\omega\rangle}{dz} = -\frac{f_R\,|\beta_2(z)|\,T(z)\pi}{4} I(z), \tag{3}$$

where

$$I(z) = \int \Im\left(\tilde{h}_R(\Omega')\right) \frac{\Omega'^3}{\sinh^2(T(z)\pi\Omega'/2)} d\Omega' \tag{4}$$

and $\Im(\tilde{h}_R)$ is the imaginary part of the Fourier transform of the Raman response, which is related to the Raman gain spectrum [22]. Then, assuming that (i) the soliton remains fundamental, (ii) confinement losses are negligible, and (iii) the photon number is conserved, it is possible to find the following evolution of the soliton duration T as a function of propagation distance z [11]:

$$T(z) = \frac{\overline{\gamma}(0)^2\,|\beta_2(z)|}{\overline{\gamma}(z)^2\,|\beta_2(0)|} T_0, \tag{5}$$

where $T_0 = T(z = 0)$ is the initial soliton temporal width. Figure 7 shows the evolution of the soliton central wavelength along propagation calculated by integrating (3) with help of (5) (red line) and by the numerical resolution of the GNLSE given by (1) (black line). A reasonable agreement is obtained between both curves, especially for the longest propagation distances (i.e., when the soliton appears to be frequency locked), the relative discrepancy on the frequency shift being less than 3% for values of z larger than 1 m. Thus, this Figure 7 shows that (i) the SSFS deceleration near the PBG edge is directly linked to the fiber properties, as claimed above and that (ii) the soliton central frequency can be predicted easily and very accurately for the longest propagation distances, without requiring the resolution of the GNLSE.

Then, in order to distinguish the effect of the spectral dependence of $\overline{\gamma}$ and the one of the spectral dependence of β_2, we now calculate the *variation* of the SSFS rate with propagation distance z. Assuming that $\beta_2 < 0$, that is, $|\beta_2| = -\beta_2$, this writes [11]

$$\frac{d^2\langle\omega\rangle}{dz^2} = \frac{f_R T(z)\pi I(z)}{4} \times \left[\frac{2\beta_2(z)}{\overline{\gamma}(z)}(4 - K(z))\frac{d\overline{\gamma}}{dz} - (3 - K(z))\frac{d\beta_2}{dz}\right], \tag{6}$$

where

$$K(z) = \frac{1}{I(z)} \int \left[\Im\left(\tilde{h}_R(\Omega')\right) - \left(\frac{d\Im\left(\tilde{h}_R\right)}{d\Omega}\right)_{\Omega'} \Omega'\right] \times \frac{\Omega'^3}{\sinh^2(T(z)\pi\Omega'/2)} d\Omega'. \tag{7}$$

From (6), it can be seen that the variation of SSFS rate during the propagation depends on the variation of β_2 and $\overline{\gamma}$ with z. Since the fiber is assumed to be invariant along its length, the variations of β_2 and $\overline{\gamma}$ with z are in fact only due to their spectral evolution as the soliton red-shifts, that is, $\beta_2\langle\omega(z)\rangle$ and $\overline{\gamma}\langle\omega(z)\rangle$. Consequently, the derivative of β_2 and $\overline{\gamma}$ with respect to z in (6) can mathematically be expressed in terms of their derivative with respect to ω. We then introduce the R ratio defined as

$$R = -\left(\frac{4 - K(z)}{3 - K(z)}\right)\frac{2\beta_2}{\overline{\gamma}}\,\frac{d\overline{\gamma}/d\omega}{d\beta_2/d\omega} \tag{8}$$

so that values of R higher than 1 indicate that the NL coefficient variation $d\overline{\gamma}/d\omega$ dominates the evolution of SSFS rate while values of R smaller than 1 mean that the dynamics of the SSFS is mainly driven by the GVD variation $d\beta_2/d\omega$, that is, by the third-order dispersion term β_3.

The blue curve of Figure 7 (right axis) shows a plot of the R ratio as a function of soliton wavelength calculated with (8). From this plot, it can be seen that the spectral variation of $\overline{\gamma}$ dominates the beginning of the SSFS dynamics, whereas for wavelengths higher than 1475 nm the effect induced by the spectral variation of β_2 becomes predominant. More importantly, the R value just below the PBG edge (located at 1535 nm) is about 0.1, which clearly means that the extreme deceleration of the SSFS is due to the large GVD slope $|\beta_3|$ near the PBG edge rather than the large NL coefficient diminution.

Finally, let us mention that, in the absence of loss, a real cancellation of the SSFS, that is, $d\langle\omega\rangle/dz = 0$, implies that β_2 and/or A_{eff} are infinite in order to get T also equal to infinite. Thus, the strong decrease of the SSFS efficiency near the PBG edge does not lead, strictly speaking, to a true suppression of the SSFS for a finite propagation distance. However, the extreme deceleration observed all along this paper is enough to consider that the soliton frequency can be considered, at least from a practical point of view, as frequency locked.

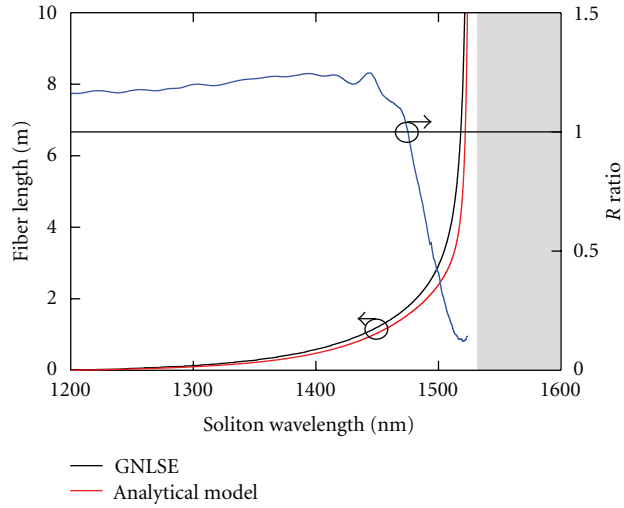

Figure 7: Left axis: evolution of the soliton central wavelength with fiber length calculated by integration of the GNLSE (black line) and with (5) in the case of the Gordon model (red line). Right axis: evolution of the R ratio defined by (8) with soliton wavelength.

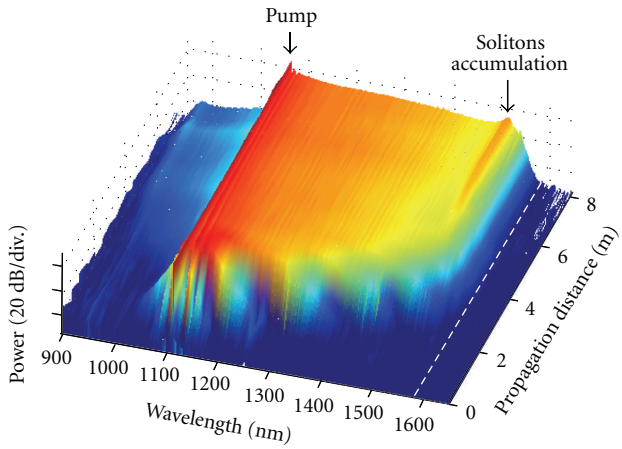

Figure 8: Experimental dynamics of the SC formation as a function of fiber length in the solid-core PBG fiber 2 for a pump power of 2.3 kW. The white dashed line represents the PBG edge.

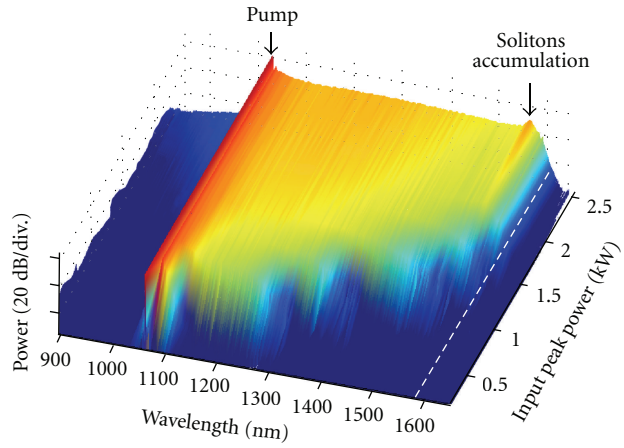

Figure 9: Experimental dynamics of the SC formation as a function of launched pump peak power. The white dashed line represents the PBG edge.

4. Tailoring the SC Extension

The SSFS is one of the main mechanisms involved in the generation of octave-spanning SC [26]. Indeed, in both the short- and long-pulse pumping regimes [27], the long-wavelength part of the SC spectrum is composed of red-shifting fundamental solitons initially created, respectively, by pulse fission and modulation instability (MI) [26]. Given that the spectral extent in the visible is intimately linked to the infrared one through a group index matching between solitons and trapped dispersive waves [28, 29], the SSFS dynamics lies at the heart of the SC generation process. There have been many attempts to optimize the spectral extension of SC sources, but, in most applications, only a small part of the SC spectrum is useful. There is thus an increasing interest in tailoring the spectral extent so that SC generation only occurs over the required spectral region. Fibers with two ZDWs have been employed in this way [30, 31]. Because the region of anomalous GVD can be suitably adjusted through a control of the microstructured cladding parameters, the SSFS can be cancelled near the long-wavelength ZDW, which results in a stop of the infrared spectral broadening. However, the SSFS cancellation is accompanied by the emission of a dispersive wave at higher wavelengths, so that the energy of frequency locked solitons exponentially decreases. In this section, we show that the cancellation of the SSFS observed in solid-core PBG fibers described above allows to control the SC spectral extent without any significant loss of energy.

4.1. Dynamics of the SC Formation. SC experiments were performed using the solid-core PBG fiber 2 of Table 1, in which long-wavelength PBG edge is located at 1580 nm. The pump laser used to generate the SC was a linearly polarized microchip laser emitting 0.6 ns pulses at 1064 nm with a repetition rate of 7 kHz. The coupling efficiency in the fibre core is estimated to be 50%. In the following, input power always refers to the power effectively launched into the fibre core.

At first, we investigated the dynamics of the SC formation with propagation distance by cutting the fiber back from 8 to 0.1 m and recording the output spectrum every 0.5 m, for a fixed pump power of 2.3 kW. Figure 8 shows the evolution of the output spectrum as a function of propagation distance. The spectrum initially presents two symmetric side lobes characteristic of MI classically observed when pumping in the anomalous GVD regime. In the temporal domain, this corresponds to the generation of a solitonic train, in which pulses strongly differ from each other in terms of peak power and duration. The spectrum then mainly broadens towards the infrared (because we pump relatively far away from the ZDW in the anomalous dispersion regime) until a fiber length of about 4 m is reached. At this propagation distance, the SC ranges from 1050 to 1580 nm. The infrared spectral broadening is due to the SSFS of each individual soliton generated from MI. Since they are characterized by very different properties, their SSFS efficiency can be very different, which leads to the SC. For further increasing fiber lengths to 8 m, the long-wavelength spectral broadening completely stops, due to the SSFS cancellation of each soliton approaching the PBG edge, following the mechanism described in Section 3. This leads to an accumulation of solitons just below the PBG edge (located at 1580 nm), which can be seen as a spectral power peak centered around 1550 nm. Consequently, the SC long-wavelength spectral extent can be tailored over a given spectral range through a suitable design of the fiber linear properties and, in particular, of the long-wavelength PBG edge.

To further illustrate this, we performed an additional experiment in which the dynamics of the SC formation was investigated as a function of pump peak power, for a fixed fiber length of 10 m. To do that, the output spectrum was recorded with 0.2 kW increments for pump peak powers ranging from 0.2 to 2.6 kW. The result of these measurements is displayed in Figure 9. Similar to previous experiments of Figure 8, the spectrum mainly broadens towards the infrared when the pump peak power is increased from 0 up to about

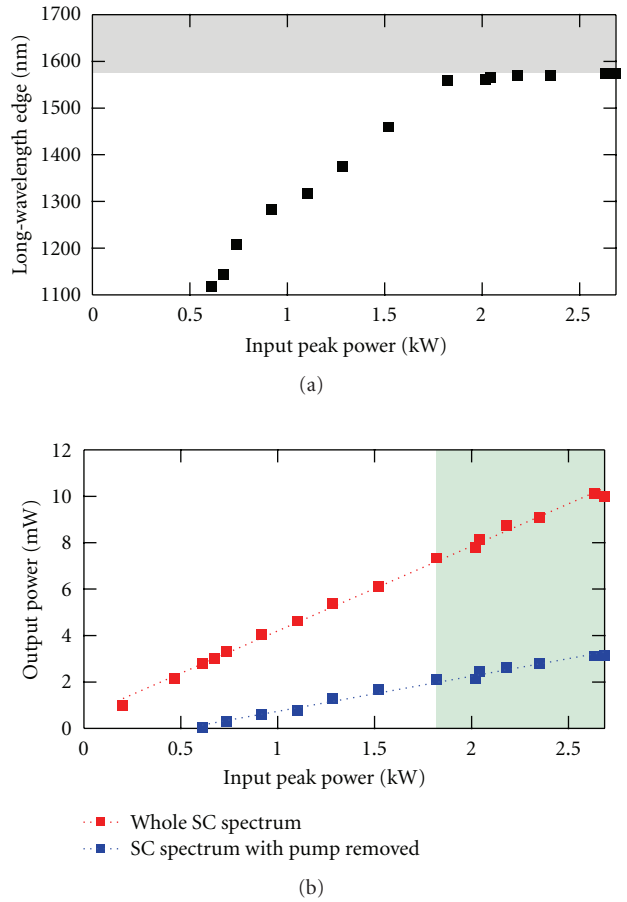

FIGURE 10: (a) Measurement of the long-wavelength edge of the SC spectrum as a function of input peak power in a 10 m-long solid-core PBG fiber sample. The gray area depicts the region outside the first PBG transmission window. (b) Measured output average power over the whole SC spectrum (red squares) and by removing the output pump peak with a 1064 nm notch filter (blue squares), as a function of input peak power. Dotted lines are linear fits. The green area corresponds to input peak powers for which the SC spectral extent stops (i.e., for input peak powers greater than 1.8 kW).

1.7 kW. For higher pump powers, the spectral broadening suddenly stops at the long-wavelength PBG edge. This is even more clearly illustrated in Figure 10(a) which represents the long-wavelength SC edge (measured for a 10 dB drop with respect to the spectral power at 1100 nm) as a function of input peak power. A clear cancellation of the spectral broadening at the PBG edge (depicted in gray) is observed for peak powers higher than 1.7 kW. As discussed above, this effect is accompanied by an accumulation of solitons which can be seen as a spectral power peak at 1550 nm, that is, just below the PBG edge located at 1580 nm.

4.2. Discussion. As shown by Figure 4 and discussed in Section 3, the SSFS cancellation occurs without any reduction of the spectral power density. This thus suggests, in the frame of SC generation, that the SC spectrum width can be limited by the PBG effect without any significant power loss. In order to check this experimentally, we plotted in Figure 10(b) the output average power measured over the whole SC spectrum (red squares) as a function of the input peak power. These measurements can be linearly fitted (red line), and the slope does not change once the SSFS cancellation has occurred and the SC spectral broadening has stopped (corresponding to the green region). In order to check that this was not due to the residual pump peak in the SC, we performed the same kind of measurements after filtering it with a notch filter at 1064 nm at the fiber output. The results are displayed with blue markers in Figure 10 and show that the output SC power (without the contribution of the 1064 nm pump) still increases with the input peak power. This confirms that the tailoring of the SC extent is not done through a simple long-wavelength filtering due to the PBG effect, which would lead to a significant output power reduction. In our case, the fact that solitons are frequency locked rather than attenuated near the PBG edge allows to keep most of the launched power into the SC and thus to optimize the pump power budget.

5. Reduction of Pulse-to-Pulse Power Fluctuations at the SC Long-Wavelength Edge

In this section, we focus our attention on pulse-to-pulse fluctuations of the SC spectral power near the long-wavelength edge of the spectrum. Indeed, in the long-pulse regime, the spectral broadening originates from the MI process which is seeded by noise and the long-wavelength SC edge is characterized by statistically rare optical rogue waves [32], originating from soliton dynamics [32–35]. Consequently, the SC is characterized by a low coherence, and pulse-to-pulse fluctuations of the spectral power at the long-wavelength SC edge are very important [32, 36]. Here, we investigate the impact of the SSFS cancellation observed in solid-core PBG fibers on pulse-to-pulse fluctuations of the long-wavelength SC edge.

5.1. Experiments. Experiments were performed using the solid-core PBG fiber 3 of Table 1, in which long-wavelength PBG edge is located at 1590 nm. Following the results of Section 4, a SC was generated using a 7 m long fiber sample and a pump power of 3 kW. Figure 11(a) shows a measurement of the spectral broadening as a function of propagation distance (made using a cutback technique). As expected, the infrared spectral broadening stops near the PBG edge, depicted with the dashed white line. Figures 11(b1) and 11(b2) shows the spectra obtained at 7 m and 2.5 m, respectively. Although the spectral extent is comparable in both cases, the shape of the spectrum is different. Indeed, while the long-wavelength edge is relatively smooth for a fiber length of 2.5 m, it becomes much sharper at 7 m, where the cancellation of the SSFS imposes a saturation of the spectral broadening. This phenomenon causes a soliton accumulation whose spectral signature is the peak located around 1560 nm, as discussed in the previous section.

Pulse-to-pulse power fluctuations of the corresponding SC obtained at 2.5 and 7 m were then studied experimentally.

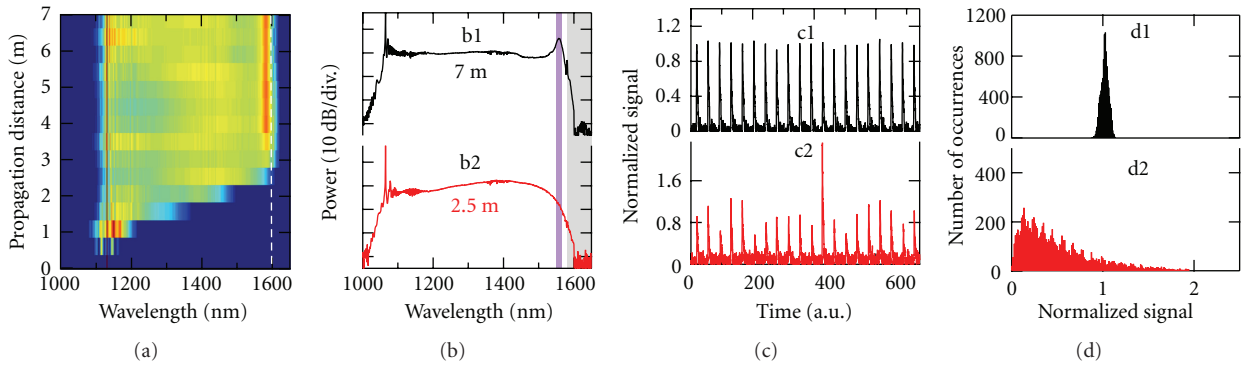

FIGURE 11: (a) Measurement of the spectral broadening as a function of propagation distance in the solid-core PBG fiber 3. The white dashed line represents the PBG edge. (b) Measured spectra for a fiber length of 7 m (b1) and 2.5 m (b2). (c1 and c2) Samples of corresponding pulse train recorded after a 10 nm bandpass spectral filtering at 1550 nm (depicted by the purple region in (b)). (d1 and d2) Corresponding statistical distribution of the signal amplitude over 10,000 records. The signal amplitude is normalized to the average over the 10,000 pulses.

To do this, the SC output was collimated and spectrally filtered with a 10 nm bandpass filter centered at 1550 nm, that is, on the soliton accumulation peak. Pulse-to-pulse fluctuations in this 10 nm wide spectral regions were measured using the method firstly proposed in [37]. The energy of spectrally filtered pulses is proportional to their peak power, so that rogue events and their associated characteristics can be captured through a simplified measurement of shot-to-shot pulse energy [37]. This was done in our experiments using a photodiode and an analog oscilloscope, with the same photodiode maximum signal amplitude and trigger level for both fiber lengths. Note that, in our experiments, this setup provides a measurement of the average energy of each pulse, but it does not allow to quantify noise-sensitive instabilities related to the actual temporal coherence of the SC, as explained in [38] for instance. The percentage of shot-to-shot variations, σ, was evaluated using $\sigma = 100 \times (V_{\max} - V_{\min})/(V_{\max} + V_{\min})$ where $V_{\max}$ and $V_{\min}$ are, respectively, the maximum and minimum photodiode signal amplitude measured at least for 10 of the 10,000 recorded pulses.

Figures 11(c1) and 11(c2) show samples of pulse trains measured for each investigated fiber length after the 10 nm bandpass filter at 1550 nm, from which pulse-to-pulse fluctuations σ can be evaluated. The pulse amplitude has been normalized to its average value over the 10,000 measurements for this plot. Pulse-to-pulse fluctuations calculated at 1550 nm are as high as 80% after 2.5 m while they drop down to 10% after 7 m. Besides, the corresponding statistical distributions at 1550 nm have very different shapes, as attested by Figures 11(d1) and 11(d2) which represent histograms calculated over 10,000 measurements for fiber lengths of 2.5 m and 7 m, respectively. The distribution is highly asymmetric after 2.5 m but becomes Gaussian-like at 7 m, that is, once solitons have reached the PBG edge. These observations thus suggest that there is a correlation between the cancellation of the SSFS occurring near the PBG edge (leading to a saturation of the SC spectrum for propagation distances longer than about 3 m), and the enhanced pulse-to-pulse stability and statistical distributions in the same spectral region.

5.2. Confirmation with Simulations. In order to get insight into these results, we performed numerical simulations using the GNLSE given by (1). At first, we simply attempted to reproduce experimental results of Figure 11. To do this, all available fiber characteristics and experimental conditions have been taken into account with no free parameter, with the exception of the pulse duration that has been reduced to 50 ps (against 600 ps in experiments). Indeed, shortening the pulse duration in simulations (while staying in the long-pulse regime though) allows to significantly reduce the computation time without significantly affecting the SC dynamics. The input pump peak power was 3 kW, and quantum noise was modeled by adding one photon per mode with random phase on each spectral discretization bin of the input field [26]. In order to study the statistical behavior of the pulse train, we performed 200 simulations with random initial noise conditions.

Simulations results are displayed in Figure 12, with the same organization as Figure 11 for easy comparison. Figures 12(a), 12(b1), and 12(b2), which show the dynamics of the SC formation, correspond to the averaged spectra over 200 simulations shots. The agreement with experiments is excellent, and the typical spectral features discussed above about the spectrum shape at its long-wavelength edge are accurately reproduced. The simulated temporal properties shown in Figures 12(c1), 12(c2), 12(d1), and 12(d2) have been calculated using a numerical gaussian filter of 10 nm (FWHM) centered at 1562 nm, which corresponds to the maximum of the spectral power peak observed near the PBG edge (see plot 12(b1)). Taking the inverse Fourier transform gives the temporal profile of the SC filtered at the corresponding wavelength, whose average power has been calculated. Samples of the modeled pulse trains corresponding to 20 simulation shots are displayed in Figures 12(c1) and 12(c2), for, respectively, fiber lengths of 7 and 2.5 m. Corresponding statistical distributions calculated from all the 200 simulations are shown in Figures 12(d1) and 12(d2) and also show excellent agreement with experiments.

All these simulation results therefore allow to reproduce not only the main spectral features observed in the

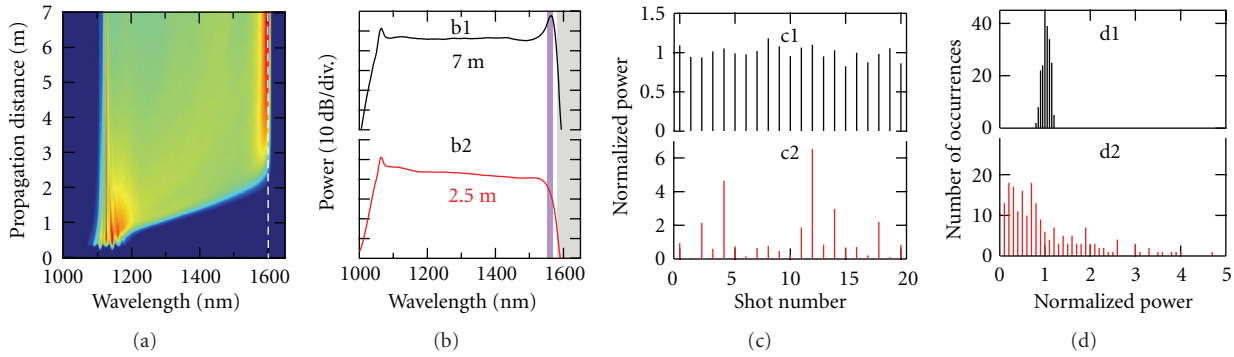

Figure 12: (a) Simulation of the spectral broadening as a function of propagation distance in the solid-core PBG fiber 3 (averaged over 200 simulation shots). The white dashed line represents the PBG edge. (b) Simulated averaged spectra for fiber lengths of 7 m (b1) and 2.5 m (b2). (c1 and c2) Samples of corresponding pulse train after spectral filtering at 1562 nm (depicted by the purple region in (b)). (d1 and d2) Corresponding histograms over 200 pulses at 1562 nm, where the power is normalized to its average over the 200 shots.

experiments (dynamics of the SC formation, typical spectral shape at the long-wavelength edge), but also the measured statistical features of the pulse train (pulse-to-pulse fluctuations as a function of wavelength and propagation distance, shape of the distribution). At this point, however, numerical simulations do not allow to discuss on the physical mechanisms responsible for the enhanced pulse-to-pulse stability near the PBG edge.

5.3. Discussion. Numerical simulations using the GNLSE accurately reproduce our experiments and can consequently be used to discuss the physical mechanisms causing the enhanced stability of the SC long-wavelength edge. To this end, the spectrotemporal representation has proved to be a powerful tool in studying the dynamics of SC generation [26]. Figures 13(a)–13(d) show the evolution of a simulated spectrogram for fiber lengths of 1, 2.5, 4, and 7 m.

Figure 13(a) shows how MI initially generates solitons that subsequently red-shifts through Raman-induced SSFS as can be seen from Figure 13(b). In such a long-pulse pumping regime, the presence of statistically rare temporal events in SC experiments can find two complementary physical origins. Firstly, it can be due to a single high peak power soliton generated from MI for particular initial noise conditions [32, 33]. Because of its higher peak power, it experiences a more efficient SSFS than other solitons and, consequently, becomes statistically rare at highest wavelengths due to the low probability for these particular noise conditions to happen [32]. Note that, in this case, the requirements for a soliton to be statistically rare at the long-wavelength SC edge, are only to experience a slightly more efficient SSFS than the other ones [39]. Secondly, following these early interpretations, it has been suggested that rare and brief events can arise from the collision of two or more solitons travelling with different group velocities [34, 35, 39, 40] because of the convective nature of the system [41]. Note that these two explanations are complementary for explaining long-tail statistical distributions usually observed at the SC long-wavelength edge [41].

In the case of the present experiments, however, this dynamics is strongly affected by the SSFS cancellation occurring near the PBG edge, as can be seen from Figures 13(c) and 13(d). Firstly, these figures show that, as long as solitons are frequency locked around 1562 nm, they all have very close group velocities at this location in the spectrum. Consequently, once they have reached the PBG edge, they cannot collide anymore, which prevents the formation of brief spikes [34] and leads to an enhanced pulse-to-pulse stability at the SC edge. Secondly, since all solitons whose SSFS has been cancelled near the PBG edge have very close characteristics, power fluctuations are reduced in this spectral region as compared to the usual case in which only a few solitons with slightly higher peak power are rare at the long-wavelength edge [32, 33].

As a consequence, the reduction of pulse-to-pulse fluctuations at the long-wavelength edge as a function of propagation distance is intimately linked to the cancellation of the SFSS discussed in Section 3. It is thus in fact due to the specific linear properties inherent to solid-core PBG fibers and, in particular, to the strong third-order dispersion near the PBG edge, as shown in Figure 3.

6. Conclusion

In conclusion, we showed that the SSFS and its dynamics can be strongly and easily manipulated thanks to the specific properties of the solid-core PBG fibers used in our various experimental and numerical studies. Indeed, we demonstrated that a quasicancellation of the SSFS could be obtained in this kind of fibers thanks to the large increase of β_2 observed on the long-wavelength edge of the first PBG. We established, trough experimental and numerical studies, that this phenomenon could be achieved without significant power loss. Thanks to these results, we demonstrated and clearly interpreted that these fibers could be used to tailor efficiently the spectral extension of SC at no power cost. Moreover, we revealed and explained that the long-wavelength edge of SC generated in this kind of fibers can present strong quantitative and qualitative differences

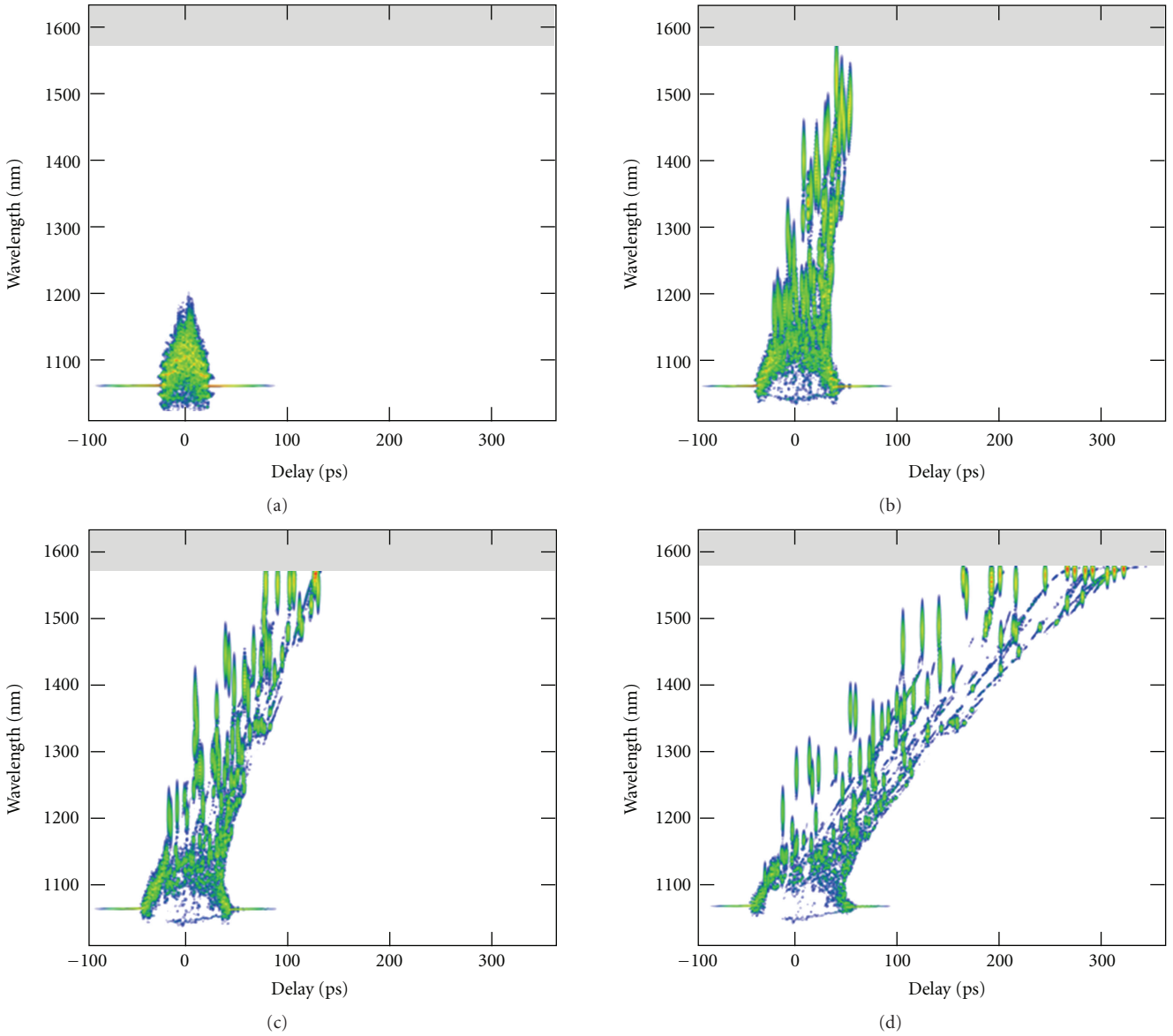

FIGURE 13: Simulated spectrograms representing the spectrotemporal dynamics of the SC generation for four propagation distances z of 1, 2.5, 4, and 7 m, respectively, from (a) to (d).

in terms of temporal stability compared to SC generated in more conventional fibres: the power fluctuations in this spectral domain are indeed strongly reduced and have a Gaussian-like statistical distribution and not the more usual L-shaped statistics associated with the presence of optical rogue waves generally observed at the long-wavelength edge of more conventional SC. We believe these results to be helpful for building SC sources for the next generation of time-resolved coherent antistokes Raman scattering (CARS) microscopes for instance [42].

Acknowledgments

The authors acknowledge Rémi Habert for experimental assistance and Karen Delplace for assistance in fiber fabrication. This work was partly supported by the French Ministry of Higher Education and Research, the Nord-Pas de Calais Regional Council, and FEDER through the "Contrat de Projets Etat Région (CPER) 2007-2013" and the "Campus Intelligence Ambiante" (CIA).

References

[1] F. Luan, A. K. George, T. D. Hedley et al., "All-solid photonic bandgap fiber," *Optics Letters*, vol. 29, no. 20, pp. 2369–2371, 2004.

[2] A. Argyros, T. A. Birks, S. G. Leon-Saval, C. M. B. Cordeiro, and P. S. J. Russell, "Guidance properties of low-contrast photonic bandgap fibres," *Optics Express*, vol. 13, no. 7, pp. 2503–2511, 2005.

[3] V. Pureur, A. Betourne, G. Bouwmans et al., "Overview on solid core photonic bandgap fibers," *Fiber and Integrated Optics*, vol. 28, no. 1, pp. 27–50, 2009.

[4] G. Bouwmans, L. Bigot, Y. Quiquempois, F. Lopez, L. Provino, and M. Douay, "Fabrication and characterization of an all-solid 2D photonic bandgap fiber with a low-loss region (< 20 dB/km) around 1550 nm," *Optics Express*, vol. 13, pp. 8452–8459, 2005.

[5] A. Fuerbach, P. Steinvurzel, J. A. Bolger, A. Nulsen, and B. J. Eggleton, "Nonlinear propagation effects in antiresonant high-index inclusion photonic crystal fibers," *Optics Letters*, vol. 30, no. 8, pp. 830–832, 2005.

[6] B. Kibler, T. Martynkien, M. Szpulak et al., "Nonlinear femtosecond pulse propagation in an all-solid photonic bandgap fiber," *Optics Express*, vol. 17, no. 12, pp. 10393–10398, 2009.

[7] A. S. Cerqueira Jr., C. M. B. Cordeiro, F. Biancalana et al., "Nonlinear interaction between two different photonic bandgaps of a hybrid photonic crystal fiber," *Optics Letters*, vol. 33, no. 18, pp. 2080–2082, 2008.

[8] P. D. Rasmussen, J. Laegsgaard, and O. Bang, "Degenerate four wave mixing in solid core photonic bandgap fibers," *Optics Express*, vol. 16, no. 6, pp. 4059–4068, 2008.

[9] A. Bétourné, Y. Quiquempois, G. Bouwmans, and M. Douay, "Design of a photonic crystal fiber for phase-matched frequency doubling or tripling," *Optics Express*, vol. 16, no. 18, pp. 14255–14262, 2008.

[10] V. Pureur and J. M. Dudley, "Nonlinear spectral broadening of femtosecond pulses in solid-core photonic bandgap fibers," *Optics Letters*, vol. 35, no. 16, pp. 2813–2815, 2010.

[11] O. Vanvincq, A. Kudlinski, A. Bétourné, Y. Quiquempois, and G. Bouwmans, "Extreme deceleration of the soliton self-frequency shift by the third-order dispersion in solid-core photonic bandgap fibers," *Journal of the Optical Society of America B*, vol. 27, no. 11, pp. 2328–2335, 2010.

[12] A. Bétourné, A. Kudlinski, G. Bouwmans, O. Vanvincq, A. Mussot, and Y. Quiquempois, "Control of supercontinuum generation and soliton self-frequency shift in solid-core photonic bandgap fibers," *Optics Letters*, vol. 34, no. 20, pp. 3083–3085, 2009.

[13] O. Vanvincq, B. Barviau, A. Mussot, G. Bouwmans, Y. Quiquempois, and A. Kudlinski, "Significant reduction of power fluctuations at the long-wavelength edge of a supercontinuum generated in solid-core photonic bandgap fibers," *Optics Express*, vol. 18, no. 23, pp. 24352–24360, 2010.

[14] A. Bétourné, G. Bouwmans, Y. Quiquempois, M. Perrin, and M. Douay, "Improvements of solid-core photonic bandgap fibers by means of interstitial air holes," *Optics Letters*, vol. 32, no. 12, pp. 1719–1721, 2007.

[15] M. Perrin, Y. Quiquempois, G. Bouwmans, and M. Douay, "Coexistence of total internal reflexion and bandgap modes in solid core photonic bandgap fibre with intersticial air holes," *Optics Express*, vol. 15, no. 21, pp. 13783–13795, 2007.

[16] M. Tateda, N. Shibata, and S. Seikai, "Interferometric method for chromatic dispersion measurement in a single-mode optical fiber," *IEEE Journal of Quantum Electronics*, vol. 17, no. 3, pp. 404–407, 1981.

[17] G. P. Agrawal, *Nonlinear Fiber Optics*, Academic Press, New York, NY, USA, 4th edition, 2007.

[18] E. M. Dianov, A. Y. Karasik, P. V. Mamyshev et al., "Stimulated-Raman conversion of multisoliton pulses in quartz optical fibers," *JETP Letters*, vol. 41, pp. 294–297, 1985.

[19] Y. Kodama and A. Hasegawa, "Nonlinear pulse propagation in a monomode dielectric guide," *IEEE Journal of Quantum Electronics*, vol. 23, no. 5, pp. 510–524, 1987.

[20] P. Beaud, W. Hodel, B. Zysset, and H. P. Weber, "Ultrashort pulse propagation, pulse breakup and fundamental soliton formation in a single-mode optical fiber," *IEEE Journal of Quantum Electronics*, vol. 23, no. 11, pp. 1938–1946, 1987.

[21] F. M. Mitschke and L. F. Mollenauer, "Discovery of the soliton self-frequency shift," *Optics Letters*, vol. 11, no. 10, pp. 659–661, 1986.

[22] J. P. Gordon, "Theory of the soliton self-frequency shift," *Optics Letters*, vol. 11, no. 10, pp. 662–664, 1986.

[23] J. Laegsgaard, "Mode profile dispersion in the generalized nonlinear Schrödinger equation," *Optics Express*, vol. 15, no. 24, pp. 16110–16123, 2007.

[24] J. C. Travers, M. H. Frosz, and J. M. Dudley, "Nonlinear fibre optics overview," in *Supercontinuum Generation in Optical Fibers*, J. M. Dudley and J. R. Taylor, Eds., chapter 3, Cambridge University Press, Cambridge, UK, 2010.

[25] D. Hollenbeck and C. D. Cantrell, "Multiple-vibrational-mode model for fiber-optic Raman gain spectrum and response function," *Journal of the Optical Society of America B*, vol. 19, no. 12, pp. 2886–2892, 2002.

[26] J. M. Dudley, G. Genty, and S. Coen, "Supercontinuum generation in photonic crystal fiber," *Reviews of Modern Physics*, vol. 78, no. 4, pp. 1135–1184, 2006.

[27] The long-pulse pumping regime refers to cases in which the pump pulse duration $\bigtriangleup T$ is much longer than the MI oscillation period $\bigtriangleup T_{\mathrm{MI}}$, given by $\bigtriangleup T_{\mathrm{MI}} = 2\pi\sqrt{|\beta_2|/(2\gamma P)}$, with β_2 the second-order dispersion coefficient, γ the NL coefficient and P the pump peak power. Cases in which $\bigtriangleup T$ is in the order or less than $\bigtriangleup T_{\mathrm{MI}}$ correspond to the short-pulse pumping regime.

[28] A. V. Gorbach and D. V. Skryabin, "Light trapping in gravity-like potentials and expansion of supercontinuum spectra in photonic-crystal fibres," *Nature Photonics*, vol. 1, no. 11, pp. 653–657, 2007.

[29] J. M. Stone and J. C. Knight, "Visibly "white" light generation in uniform photonic crystal fiber using a microchip laser," *Optics Express*, vol. 16, no. 4, pp. 2670–2675, 2008.

[30] A. Kudlinski, G. Bouwmans, Y. Quiquempois, and A. Mussot, "Experimental demonstration of multiwatt continuous-wave supercontinuum tailoring in photonic crystal fibers," *Applied Physics Letters*, vol. 92, no. 14, Article ID 141103, 2008.

[31] A. Kudlinski, G. Bouwmans, M. Douay, M. Taki, and A. Mussot, "Dispersion-engineered photonic crystal fibers for CW-pumped supercontinuum sources," *Journal of Lightwave Technology*, vol. 27, no. 11, pp. 1556–1564, 2009.

[32] D. R. Solli, C. Ropers, P. Koonath, and B. Jalali, "Optical rogue waves," *Nature*, vol. 450, no. 7172, pp. 1054–1057, 2007.

[33] J. M. Dudley, G. Genty, and B. J. Eggleton, "Harnessing and control of optical rogue waves in supercontinuum generation," *Optics Express*, vol. 16, no. 6, pp. 3644–3651, 2008.

[34] A. Mussot, A. Kudlinski, M. Kolobov, E. Louvergneaux, M. Douay, and M. Taki, "Observation of extreme temporal events in CW-pumped supercontinuum," *Optics Express*, vol. 17, no. 19, pp. 17010–17015, 2009.

[35] G. Genty, C. M. de Sterke, O. Bang, F. Dias, N. Akhmediev, and J. M. Dudley, "Collisions and turbulence in optical rogue wave formation," *Physics Letters, Section A*, vol. 374, no. 7, pp. 989–996, 2010.

[36] F. Vanholsbeeck, S. Martin-Lopez, M. González-Herráez, and S. Coen, "The role of pump incoherence in continuous-wave supercontinuum generation," *Optics Express*, vol. 13, no. 17, pp. 6615–6625, 2005.

[37] C. Lafargue, J. Bolger, G. Genty, F. Dias, J. M. Dudley, and B. J. Eggleton, "Direct detection of optical rogue wave energy

statistics in supercontinuum generation," *Electronics Letters*, vol. 45, no. 4, pp. 217–219, 2009.

[38] H. Kubota, K. R. Tamura, and M. Nakazawa, "Analyses of coherence-maintained ultrashort optical pulse trains and supercontinuum generation in the presence of soliton-amplified spontaneous-emission interaction," *Journal of the Optical Society of America B*, vol. 16, no. 12, pp. 2223–2232, 1999.

[39] M. Erkintalo, G. Genty, and J. M. Dudley, "On the statistical interpretation of optical rogue waves," *European Physical Journal*, vol. 185, no. 1, pp. 135–144, 2010.

[40] K. Hammani, B. Kibler, C. Finot, and A. Picozzi, "Emergence of rogue waves from optical turbulence," *Physics Letters, Section A*, vol. 374, no. 34, pp. 3585–3589, 2010.

[41] M. Taki, A. Mussot, A. Kudlinski, E. Louvergneaux, M. Kolobov, and M. Douay, "Third-order dispersion for generating optical rogue solitons," *Physics Letters, Section A*, vol. 374, no. 4, pp. 691–695, 2010.

[42] D. A. Sidorov-Biryukov, E. E. Serebryannikov, and A. M. Zheltikov, "Time-resolved coherent anti-Stokes Raman scattering with a femtosecond soliton output of a photonic-crystal fiber," *Optics Letters*, vol. 31, no. 15, pp. 2323–2325, 2006.